HOKKAIDO UNIVERSITY

| | |
|---|---|
| Title | Saroma-ko Lagoon Observations for sea ice Physico-chemistry and Ecosystems 2019 (SLOPE2019) |
| Author(s) | Nomura, Daiki; Wongpan, Pat; Toyota, Takenobu et al. |
| Citation | Bulletin of Glaciological Research, 38, 1-12<br>https://doi.org/10.5331/bgr.19R02 |
| Issue Date | 2020-03-31 |
| Doc URL | https://hdl.handle.net/2115/79060 |
| Rights | 著作権は日本雪氷学会にある |
| Type | journal article |
| File Information | 38_19R02.pdf |

Hokkaido University Collection of Scholarly and Academic Papers : HUSCAP

Bulletin of Glaciological Research 38 (2020) *1–12*
doi: 10.5331/bgr.19R02
©Japanese Society of Snow and Ice


# Saroma-ko Lagoon Observations for sea ice Physico-chemistry and Ecosystems 2019 (SLOPE2019)

**Daiki NOMURA[1,2,3]*, Pat WONGPAN[4,5], Takenobu TOYOTA[4], Tomonori TANIKAWA[6], Yusuke KAWAGUCHI[7], Takashi ONO[4], Tomomi ISHINO[1], Manami TOZAWA[1], Tetsuya P. TAMURA[1], Itsuka S. YABE[7], Eun Yae SON[7], Frederic VIVIER[8], Antonio LOURENCO[8], Marion LEBRUN[8], Yuichi NOSAKA[9], Toru HIRAWAKE[1,2], Atsushi OOKI[1,2], Shigeru AOKI[4], Brent ELSE[10], Francois FRIPIAT[11], Jun INOUE[12] and Martin VANCOPPENOLLE[8]**

1 Faculty of Fisheries Sciences, Hokkaido University, Hakodate, Japan
* daiki.nomura@fish.hokudai.ac.jp (corresponding author)
2 Arctic Research Center, Hokkaido University, Sapporo, Japan
3 Global Station for Arctic Research, Global Institution for Collaborative Research and Education, Hokkaido University, Sapporo, Japan
4 Institute of Low Temperature Science, Hokkaido University, Sapporo, Japan
5 JSPS International Research Fellow, Japan Society for the Promotion of Science, Tokyo, Japan
6 Meteorological Research Institute, Japan Meteorological Agency, Tsukuba, Japan
7 Atmosphere and Ocean Research Institute, The University of Tokyo, Tokyo, Japan
8 Sorbonne Université, Laboratoire d'Océanographie et du Climat/Institut Pierre-Simon Laplace, CNRS/IRD/MNHN, Paris, France
9 School of Biological Sciences, Tokai University, Sapporo, Hokkaido, Japan
10 University of Calgary, Calgary, Canada
11 Max Planck Institute for Chemistry, Mains, Germany
12 National Institute of Polar Research, Tokyo, Japan

(Received August 21, 2019; Revised manuscript accepted February 25, 2020)

## Abstract

Saroma-ko Lagoon, located on the Okhotsk Sea coast of Hokkaido, is seasonally covered by flat, homogeneous, easily accessible and safe sea ice. As such, it proves a very useful experimental site for the study of sea ice processes, the inter-comparison of methods, the testing of equipment, and the training of researchers new to the Polar regions. In this contribution, we describe a physical, chemical, and ecosystem survey at Saroma-ko Lagoon, conducted over February 23–28, 2019 under the auspices of the SLOPE2019 (Saroma-ko Lagoon Observations for sea ice Physico-chemistry and Ecosystems 2019) program. Sea ice cores were collected to examine temperature, salinity, oxygen isotopic ratio, thin sections, and chemical and biological parameters such as carbonate chemistry, $CH_4$, nutrients, chlorophyll *a* concentrations, and ice algae community assemblage. Broadband and spectral irradiance measurements were carried out above/under the sea ice, and different sensors were inter-compared at close positions and environments. Equipment such as spectrometers, air–sea ice $CO_2$/$CH_4$ flux chamber, and under-ice turbulent heat flux systems were tested for future Arctic and Antarctic expeditions. Finally, an artificial pool was dug into the sea ice to understand the effect of snow particles on ice growth and to compare the gas exchange process over sea ice with an ice-free water surface. Our SLOPE2019 field campaign activities provided useful information for inter-comparison work and future sea ice research in the polar oceans.

Key words: sea ice, light, training and test measurement, inter-comparison, Saroma-ko Lagoon

## 1. Introduction

Saroma-ko Lagoon (surface area, 151.59 $km^2$ and maximum depth, 22 m) is located on the northeast coast of Hokkaido, Japan, and is connected to the southern part of the Sea of Okhotsk through two inlets. Saroma-ko Lagoon and the surrounding areas are located at the lowest-latitude where sea ice forms in the northern hemisphere (*e.g.* Liu *et al.*, 2018). The water mass of the eastern part of the lagoon consists mainly of Okhotsk Sea water with freshwater input from the Saromabetsu River (Shirasawa and Leppäranta, 2003; Nomura *et al.*, 2009, 2010). Almost the entire surface of the lagoon is covered with sea ice from early January through early April (Shirasawa and Leppäranta, 2003; Shirasawa *et al.*, 2005). Because the sea ice forms in a semi-enclosed lagoon protected from dynamical disturbance, the sea ice

conditions are kept almost stable which produces flat and homogeneous land-fast ice, and thus provide safe and comfortable conditions for sea ice research. This also provides good conditions for training students and researchers, and for equipment testing in conditions easier and safer than in the context of Southern or Arctic Ocean field work. International sea ice field courses for interdisciplinary sea-ice research have been carried out in collaboration with USA, Finland, and Australia.

Observations over recent decades suggest that sea ice plays a significant role in the biogeochemical cycles within polar seas and oceans, providing an active biogeochemical interface at the ocean-atmosphere boundary (Vancoppenolle *et al*., 2013). However, a pressing need exists to perform methodological inter-comparison experiments in order to obtain reliable measurements of basic biogeochemical properties (Miller *et al.*, 2015). With newly emerging techniques, and pressed by the rapid changes in sea ice, the time has come to evaluate and improve our approach to study sea-ice systems. In 2016, the Scientific Committee on Oceanic Research (SCOR) launched Working Group 152 on Measuring Essential Climate Variables in Sea Ice (ECV-Ice). This working group will synthesize past inter-comparison exercises and design and coordinate new experiments. The ultimate goal is to provide the international community with standardized protocols for processing sea-ice samples and collecting data for key variables. Saroma-ko Lagoon is especially suited for inter-comparison experiments of sea ice measurement methods. So far inter-comparison experiments conducted in Saroma-ko Lagoon focused on the effect of melting treatments on the assessment of biomass and nutrients in sea ice in 2016 (Roukaerts *et al*., 2019) and sea ice primary production in 2018.

Sea ice is an optical medium controlling light availability for sympagic and pelagic ecological communities including sea ice algae (Horner *et al*., 1988; Arrigo, 2017). Optical properties within sea ice and under-ice water is affected by the ice surface properties including snow, sea ice physics (*e.g.*, brine channel network and sea ice structure) and biogeochemistry (*e.g.*, ice algae biomass). The amount of ice algae biomass is also related to nutrient availability within sea ice and under-ice water. Therefore, in order to understand the optical properties within sea ice, a physical, chemical, and ecosystem survey is needed. In previous studies at the Saroma-ko Lagoon, spatial and temporal approaches for physical and biogeochemical research have been examined (Robineau *et al*., 1997, Liu *et al*., 2018). In addition, model approach to understand the biogeochemical cycles of sea ice were also developed (Nishi and Tabeta, 2005).

Bio-optical observations of hyperspectral light transmission under sea-ice has been studied and has yielded new techniques for non-invasive estimates of sea ice algal biomass in the polar oceans (*e.g.*, Campbell *et al*., 2015; Lange *et al*., 2016; Melbourne-Thomas *et al*., 2016; Lund-Hansen *et al.*, 2018; Wongpan *et al*., 2018). However, studies are very limited in non-polar sea ice, *e.g.*, the Baltic Sea (Granskog *et al*., 2004; Uusikivi *et al.*, 2010) or Saroma-ko Lagoon (Robineau *et al*., 1997).

The purpose of the 2019 campaign was to 1) examine the physical, chemical, and ecosystems of sea ice and snow for light measurement above/under the sea ice, 2) inter-compare different light measurement methods performed with different sensors, 3) test equipment for future Arctic and Antarctic expeditions, such as spectroradiometers, air–sea ice $CO_2$/$CH_4$ flux chamber, and under-ice turbulent heat flux systems, 4) document the link between meteorological conditions and ice crystal alignment in young sea ice, 5) compare gas exchange processes over sea ice and an ice-free water surface by using artificial pool, and 6) train and educate students and young scientists for future polar expeditions.

## 2. Sampling site and environmental conditions

Field work was conducted from February 23 to 28, 2019 by several sub-groups organized around different locations near 44°07′08″N, 143°56′56″E, 2 km from the eastern coast of the Saroma-ko Lagoon, Hokkaido, Japan (Fig. 1). Snow depth was 8.4±1.2 cm (n=150) and sea ice thickness was 47.5±3.2 cm (n=30), whereas water depth was about 6 m. In this paper, we used local time (UTC+9 hour).

To understand environmental conditions during this campaign, we monitored temperature and wind in the air. Air temperature, and wind direction and speed were monitored at one minute intervals by the automatic weather system (AWS) (Kestrel manufacturer) at site C2 with accuracies of 0.5℃ for air temperature and 3% of reading for wind speed. Air temperature ranged from −15℃ to +2℃ during the observation period (Fig. 2a) and featured a clear day-night cycle. Southerly to westerly wind dominated with wind speed ranging from 0 to 5 m $s^{-1}$. Wind data were not obtained at night, presumably owing to freezing of the propeller. Yet, since daytime wind speed was consistent with the nearby Tokoro weather station (Fig. 1c) and run by the Japan Meteorological Agency (Fig. 2b), the wind data at the latter site were used for analysis. Upward and downward radiative fluxes, including shortwave and longwave radiation, were monitored at one minute intervals by a radiometer (MR-40, EKO Instruments Co., Ltd) near the AWS (Fig. 3a).

Light conditions during SLOPE2019 were typically beautiful weather, clear skies, with occasional cirrostrati and cirrocumuli, and rarely full overcast conditions. The last day (28 February 2019) was entirely free of clouds. Every day, near sunset (around 18:00), the solar disk was disappearing behind the mountains and the moon was showing up, from waning gibbous to last quarter (81–51% of visible moon disk).

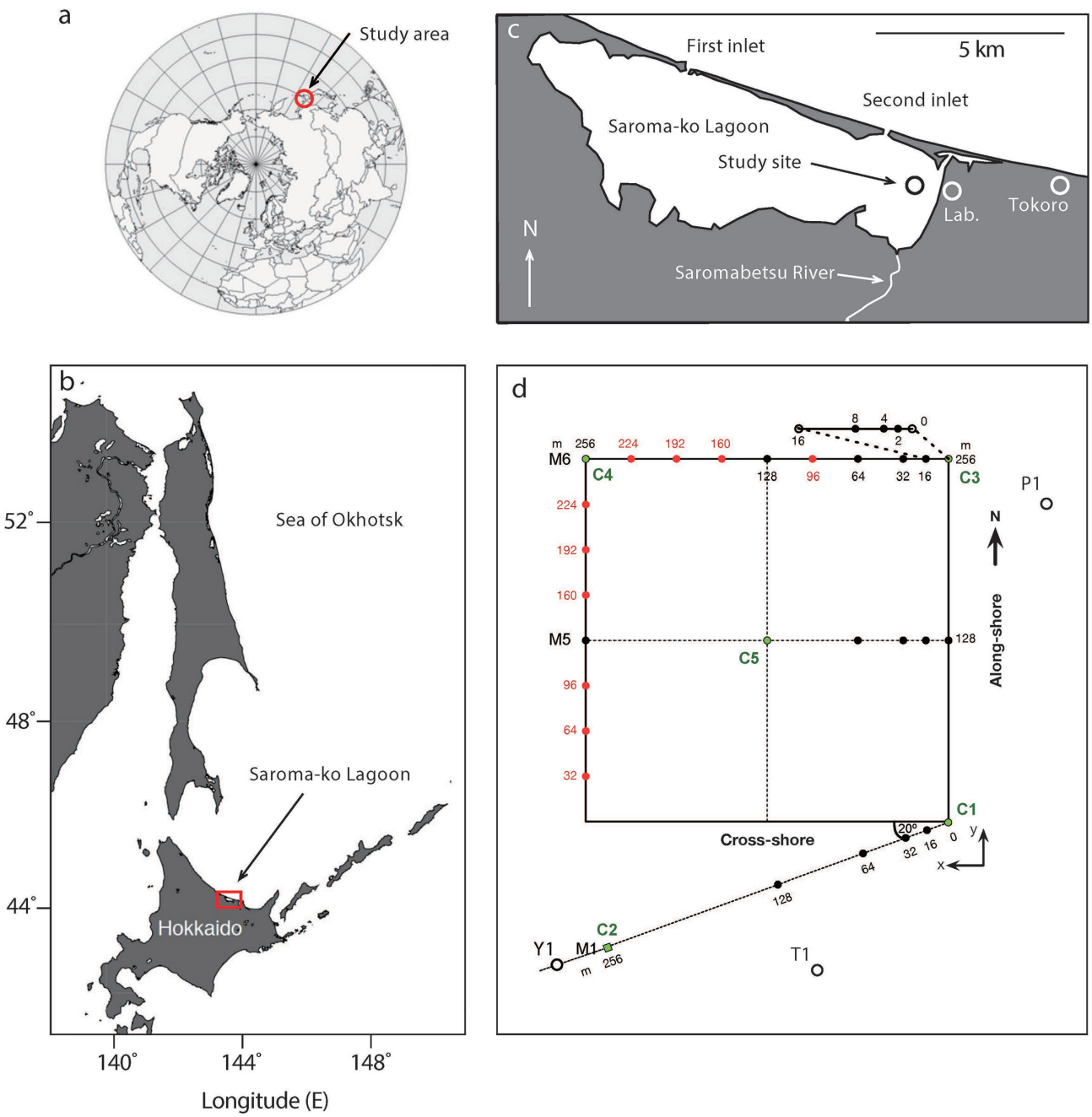


Fig. 1. Location map of the Sea of Okhotsk (a), Saroma-ko Lagoon (b), study site within the lagoon (c), and sea ice site coordination during SLOPE2019 (d).

## 3. Sea ice and snow properties

In order to understand the sea ice and snow properties which were related to the optical properties of sea ice, we collected sea ice cores, and examined physical, chemical, and ecosystems of the sea ice. Sea ice cores and overlying snow were sampled at site C2 on 23 (16:00), 25 (15:45), and 27 February 2019 (15:49). Sea ice cores were taken using a standard sea ice corer (Mark II coring system, Kovacs Enterprises, Inc.). Snow was sampled using a plastic shovel. Vertical temperature profiles within ice core and snow were inferred from a needle temperature probe (Testo 110 NTC, Brandt Instruments, Inc.). Ice cores were then cut every 10 cm from the bottom of the ice. Snow samples and sea ice core sections were placed into the air-tight Smart bags PA (AAK 5 L, GL Sciences Inc.) and melted in the dark at +4℃. After melting, meltwater was poured in the bottles for each parameter, and samples were processed/analyzed.

Figure 4 shows the vertical profile of temperature, salinity, brine volume fraction, carbonate chemical parameters such as dissolved inorganic carbon (DIC) and total alkalinity (TA), and chlorophyll *a* (chl. *a*) concentrations within sea ice and snow (other parameters such as water oxygen isotopic ratio, $CH_4$, and nutrients are currently being processed and analyzed). Vertical temperature profiles in sea ice were remarkably stable

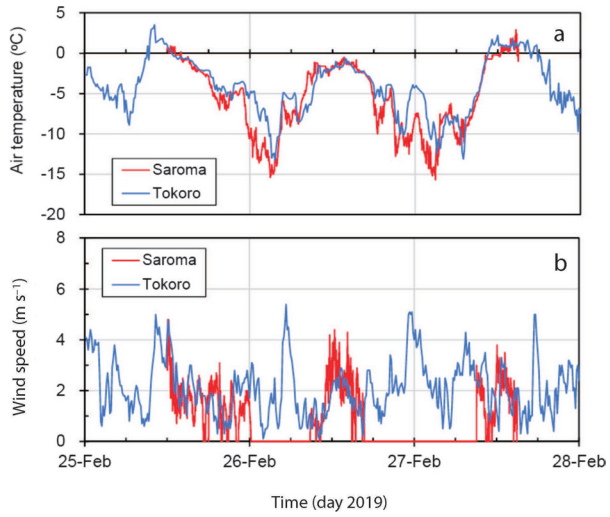


Fig. 2. Time series of air temperature (a) and wind speed (b) at Saroma-ko Lagoon (red) and the weather station in Tokoro (blue) (Fig. 1c).

through the experiment (Fig. 4a). By contrast snow temperature profiles were more variable (Fig. 4a). This is because the specific heat of saline ice is much higher than that of snow, buffering temperature changes in sea ice. The variability in snow temperature reflects changes in sampling time combined with a strong air temperature diurnal cycle. High salinities (S>17 psu) characterized the bottom of the snow and the sea ice surface, and the profile within the sea ice was C-shaped (Fig. 4b). Brine volume fraction of sea ice calculated from the temperature and salinity ranged from 8 to 30 % (Fig. 4c), indicating permeable sea ice. Vertical profiles of DIC and TA were similar with that of salinity and ranged from 42 to 1159 μmol $kg^{-1}$ for DIC and 26 to 1305 μmol $kg^{-1}$ for TA (Figs. 4d and e). Chl. *a* concentration was high at the bottom of the sea ice (>166 μg $L^{-1}$) (Fig. 4f), and these concentrations were higher than typically observed at the site (Nomura *et al.*, 2011) presumably due to the low snow depth during this campaign and higher light penetration through the snowpack and sea ice. Basically, there was no temporal variation during the ice sampling period (within 5 days) for each parameter, except for the temperature within the snowpack (the variability in snow temperature was affected by a strong air temperature diurnal cycle). The vertical thin-section photographs of the sea ice core at site C2 on 25 February 2019 (Fig. 4g) indicated that most of the ice core was dominated by the granular ice (snow-ice plus frazil ice) (89 % of the ice thickness in the upper parts of the ice core), and columnar ice made up to 11 % of the lower parts of the core. The sea-ice algal community was overwhelmingly dominated by diatoms (98 %, cell counts) (Fig. 5) and the remaining were cryptophytes and dinoflagellates.

Snow analyses were conducted at sites T1 and T2, including snow classification and measurements of snow depth, grain size, density, temperature, and mass concentrations in impurities. Figure 6 shows an example

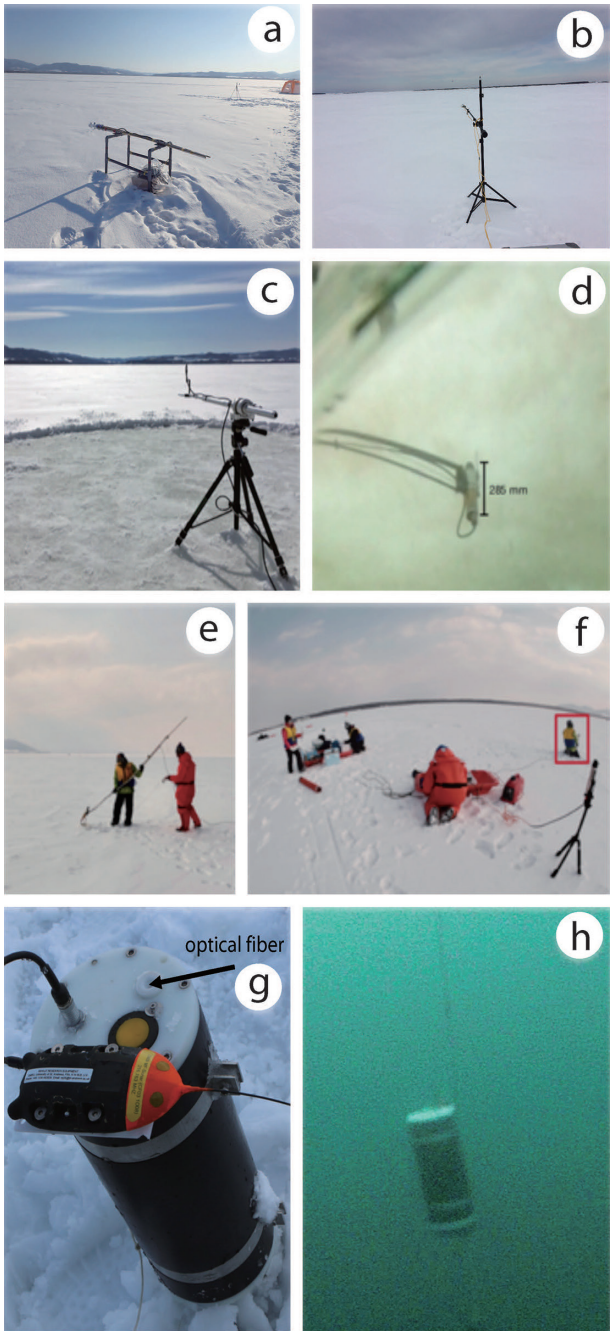


Fig. 3. Photograph of MR-40 (a), CNR4 (b), FieldSpec FR (c), under-ice irradiance sensor measuring the light transmits through snow, sea ice, and is absorbed by sea ice algae (d). The irradiance sensor was installed through the borehole (e), and the above-ice sensor and under-ice while the temperature of the drilled core was measured in concert (f). Photograph of STS-VIS (g) and STS-VIS in the water (h).

of the snow conditions in the sampling layers. At site T1, the snowpack of 7 cm depth was spread over the sea ice of approximately 51 cm. The observed snow form in the upper layers consisted of rounded grains of $r_1$ ~400 μm and $r_2$ ~100 μm (median) while the lower layers mainly consisted of melt forms of $r_1$ ~1500 μm and $r_2$ ~600 μm (median) corresponding to the snow grain size where two measures of snow grain size were measured (Tanikawa *et al.*, 2014). The temperatures of snow were all below

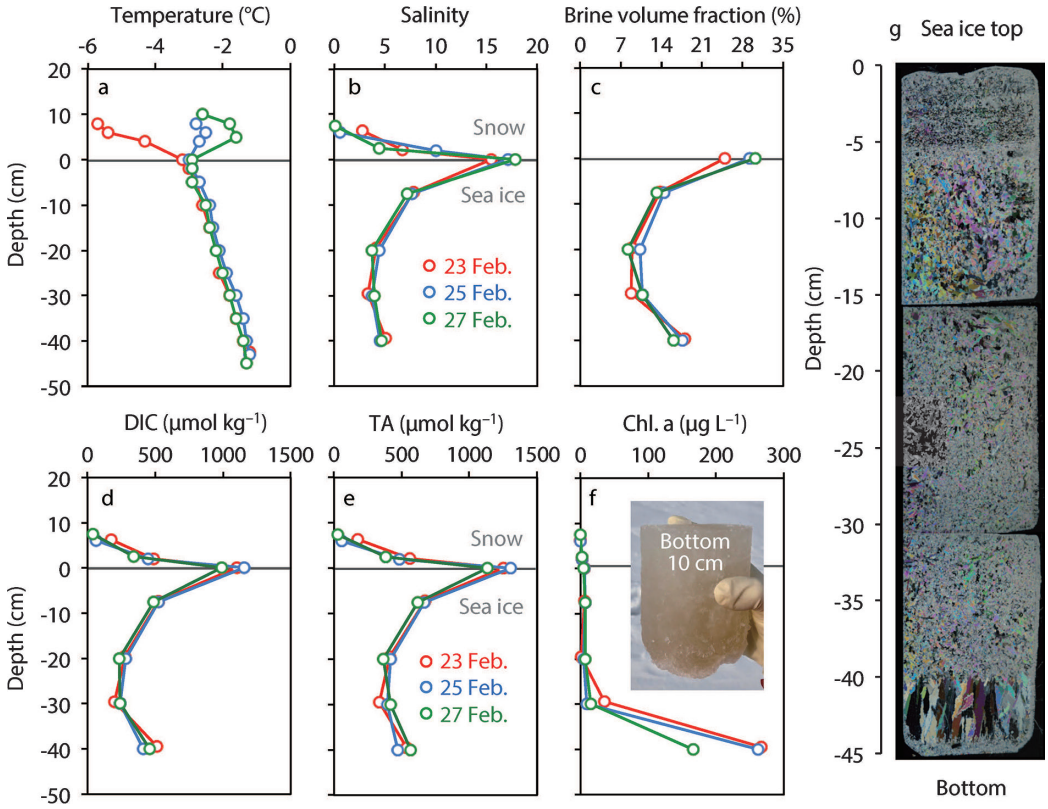


Fig. 4. Vertical profile of temperature (a), salinity (b), brine volume fraction (c), carbonate chemical parameters such as dissolved inorganic carbon (DIC) (d) and total alkalinity (TA) (e), and chl. *a* concentrations (f) within sea ice and snow at site C2 at 23, 25, and 27 February 2019. The picture in f shows the bottom ice section of the ice core at site C2. The vertical thin-section photographs of the sea ice core at site C2 at 25 February 2019 (g).

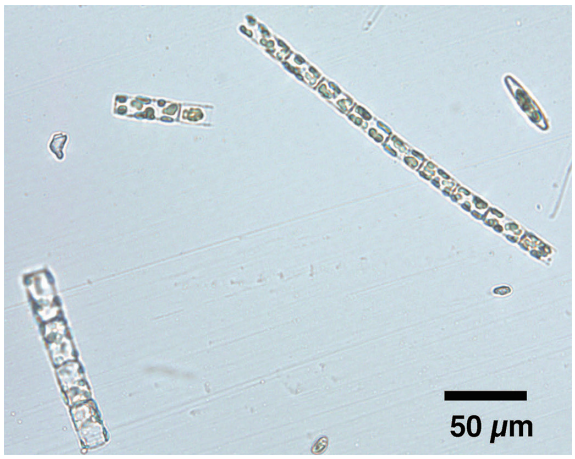


Fig. 5. Photographic image of ice algae community assemblage for bottom ice section of the ice core from site C2. Cell counting for ice algae community assemblage was examined with a microscope (IMT-2, Olympus) 10× oculars and 40× objective.

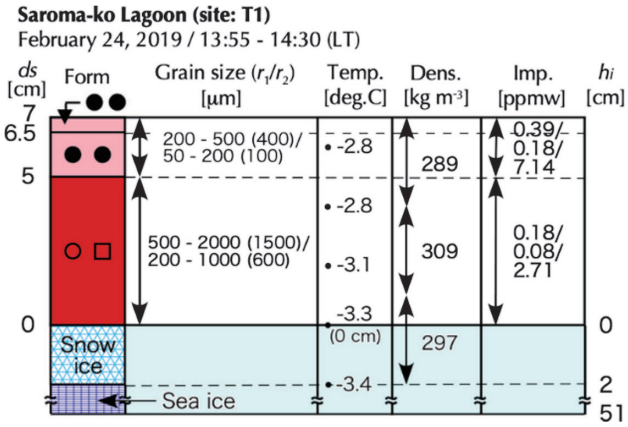


Fig. 6. Vertical profiles of snow parameters obtained from snow pit work at 24 February 2019 at site T1. The ds and hi are snow depth and sea ice thickness, respectively. The characters used to indicate snow form are in accordance with the snow classification scheme of Fierz *et al.* (2009). For snow grain size, statistics of minimum, maximum and medium (number within brackets) are indicated. Two dimensions of grain size were defined: one half the length of the major axis of dendrites or cluster of aggregated grains ($r_1$) and one-half the branch width of dendrites, which is half of the width of the narrower part of broken crystals or the radius of each spherical particle ($r_2$). Snow impurities has three values, OC, EC, and dust, respectively.

freezing. Snow density was approximately 300 kg m$^{-3}$. The mass concentrations of snow impurity of organic carbon, elemental carbon, and dust were 0.39, 0.18, and 7.14 for a top layer and 0.18, 0.08, and 2.71 for a bottom layer, respectively. Technical details of snow analyses were described in Tanikawa *et al.* (2014) and Kuchiki *et al.* (2015).

## 4. Optical measurements above/under the sea ice

Optical properties above/under the sea ice are strongly related to the albedo, the algal communities at the bottom of the sea ice and the under-ice water. In order to measure the optical properties above/under the sea ice, there are various type of methods and sensors. In this study, optical measurements were performed above and under the ice by three different sub-groups. This included broadband and spectral measurements, above and under sea ice, and this section gives an overview of the instruments deployed and measurements performed. These provide a detailed view of the light field above and under the sea ice. Inter-comparison of the different instruments deployed provides additional insights on uncertainties. All measurements have in common that care was taken to minimize the footprints and shadow effects.

### *4.1 Optical and ancillary measurements*

#### *4.1.1 Pyranometers (broadband radiation)*

Broadband, near-surface, planar irradiances, in their down- and up-welling shortwave (SW) and longwave components, were collected with two different instruments: the MR-40 (EKO Instruments Co., Ltd) (Fig. 3a), and the CNR4 (Kipp and Zonen, Delft) (Fig. 3b). Both instruments were deployed at about 30 m from each other, near site C2 (see Fig. 1). Both instruments have slightly different spectral range: 285 nm–3 μm for MR-40 and 305 nm–2.8 μm for CNR4. The MR-40 was mounted on a table-shaped stand (Fig. 3a). The CNR4 was mounted on a tripod with a 2-m arm extension (Fig. 3b). Broadband albedo was retrieved by dividing the upwelling by downwelling irradiance. Because of radiometer errors at low irradiance and solar angles and of concomitant drastic changes in albedo, we used a threshold of 50 W $m^{-2}$ on incoming irradiance to calculate albedo. Both instruments were deployed during the full survey, starting on 23 February 2019, slightly after solar noon and ending on 27 February 2019, in the afternoon. CNR4 failed on the last measurement day (27 February 2019). Three full daily cycles were captured by both instruments. Both instruments sampled at 1 minute resolution.

#### *4.1.2 Spectrometers and spectral radiometers (spectral radiation)*

A second set of experiments was focused on spectral measurements above and under the sea ice. Three different instruments were used for specific purposes and deployed at distinct locations. Occasionally, they were also deployed jointly during several short inter-comparison sessions.

(i) The FieldSpec FR grating spectrometer (PANalytical) was mostly used to measure surface spectral albedo. The FieldSpec FR covers $\lambda$=0.35–2.5 μm, with a spectral resolution of 3 nm for $\lambda$=0.35–1.0 μm; and of 10 nm for $\lambda$=1.0–2.5 μm. To integrate over a half-sphere and measure irradiance, a cosine collector was used. The latter consisted of a white reference standard of a Spectralon diffuser panel, SRT-90 (Labsphere). The spectral upwelling and downwelling irradiance fluxes were retrieved, from which spectral albedo was deduced. The FieldSpec FR was deployed at sites T1 and T2 (200 m away from the eastern coast of Saroma-ko Lagoon) (Fig. 3c).

(ii) Two TriOS RAMSES ACC UV/VIS hyperspectral radiometers (SAM 8182 and SAM 8033, TriOS) were used for a spatial survey of under-ice spectral light transmission (Figs. 3d–f). The TriOS RAMSES covers a wavelength range of 350 to 920 nm, with spectral resolution of 3.3 nm. Protocols from Wongpan *et al.* (2018) were applied. A first sensor (SAM 8182) was deployed above the sea ice, mounted on a tripod at about 1 m height (Fig. 3f). A second sensor (SAM 8033) was deployed under the ice using a retractable L-arm (Fig. 3d). The L-arm was inserted through a 0.11 m (diameter) borehole drilled with the Mark II Kovacs corer. The horizontal arm was 1.3 m long, and the sensor was placed ~7.5 cm below the ice–ocean interface. The two sensors were connected to a laptop using the IPS104-4 Plus interface (Fig. 3f). The MSDA software was used, enabling synchronous measurements above and under the sea ice. Specific calibration files were used for the above- (air) and under-sea ice (water) measurements. At least three joint above- and under-ice spectra were recorded at each measurement location. Finally, spectral transmittance was retrieved from the ratio of under- and above-ice downwelling planar irradiant fluxes.

Once done the optical measurements, snow and ice sampling for biogeochemical parameters were started. The location of the under-ice radiometer and snow depth were recorded. Snow samples were collected in a Ziploc bag. A sea ice core was taken and sliced into bottom 0.1 m, and equal-length middle and top sections. The melting of snow and ice samples, filtration and measurement of chl. *a* concentration (Turner Designs 10AU Field and Laboratory Fluorometer) were done following standard protocol (*e.g.* Roukaerts *et al.* 2019) by melting without addition of filtered seawater at low temperature (around +5℃) in the dark. Optical measurements with the TriOS RAMSES spectrometers, and sampling of snow and ice core were performed at 27 sites over a 250 m×250 m area (see Fig. 1d), from 23 to 26 February 2019. The sampling sites were located on three east-west lines at 0, 2, 4, 8, 16, 32, 64, 128, and 256 m. The three lines were separated by 128 m in the south-north direction.

(iii) An STS-VIS grating micro-spectrometer (Ocean Optics), was deployed in the framework of a temporal survey of under-ice spectral light transmission (Fig. 3g). The STS-VIS photodiode array covers the 350–800 nm wavelength range, with 1024 channels. As the effective spectrometer resolution is ~10 nm, a 30-channel smoothing was applied to all outputs. The STS-VIS was deployed under the ice, onboard the Ice-T *fish* system, an ice-tethered sealed cavity hanging below the ice at depth up to 5 m, and

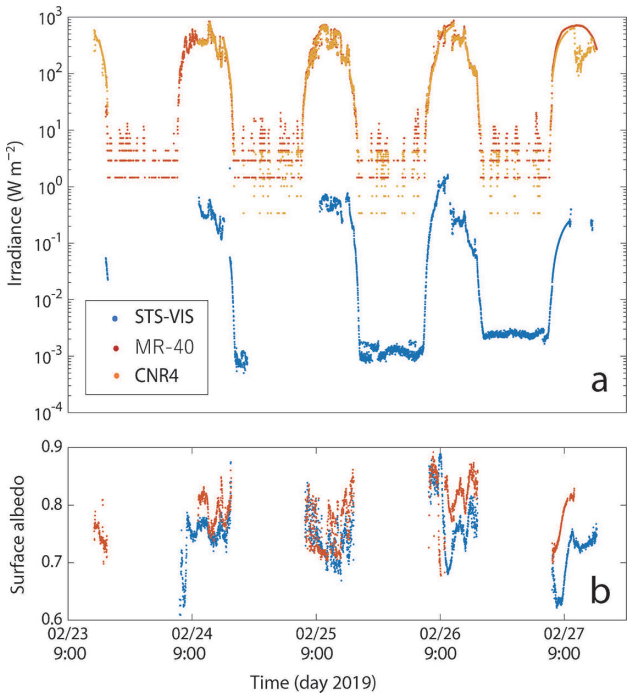


Fig. 7. Time series of downwelling planar irradiance from different instruments (MR-40 and CNR4 above the ice surface and STS-VIS under the ice surface at about 5 m depth) (a). Time series of surface albedo diagnosed from MR-40 and CNR4 (b).

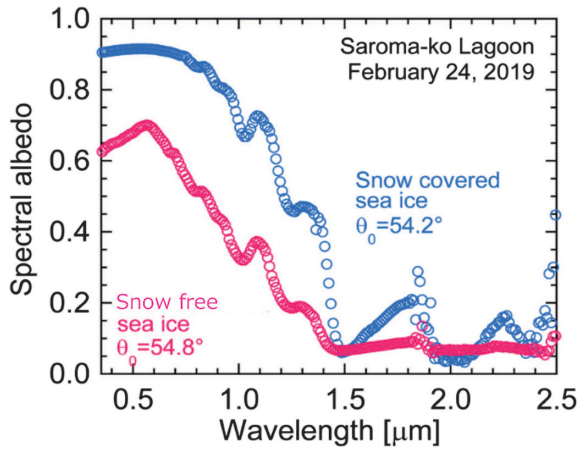


Fig. 8. Spectral albedos for snow covered- and -free sea ice, respectively. $\theta_0$ is solar zenith angle.

inclined with an angle of 10–20°, depending on current intensity (Fig. 3h). An optical fiber placed through the upper lid of the Ice-T *fish* connects the STS-VIS to the exterior. Radiances (W m$^{-2}$ nm$^{-1}$) were retrieved from counts, then converted to irradiances assuming an elliptical angular radiance distribution in the water column. Irradiance over the visible range is finally computed by wavelength-integration.

The STS-VIS was deployed at site C2 during February 23–24, 2019 and taken home at night, to ensure proper data collection. On 25 February 2019, the STS spectrometer was deployed at site C4 and left under water, during two complete days and nights.

### *4.2 Above-ice measurements: irradiance and albedo*

#### *4.2.1 Solar irradiance above sea ice*

Time series of incoming solar irradiance from the MR-40 and CNR4 show the expected solar irradiance diurnal cycle (Fig. 7a). During daytime, irradiance typically was within the range of 0–600 W m$^{-2}$. At night, irradiance was within the range of 0.5–20 W m$^{-2}$. This suggests substantial light pollution, since a full moon would irradiate at $10^{-3}$ W m$^{-2}$. By all means, the amount of noise suggests that the detection limits of both MR-40 and CNR4 are reached at night.

MR-40 and CNR4 can be compared when simultaneously operational. Both instruments suggest extremely consistent irradiance variations at temporal scales as small as 1 minute. There are systematic differences between both instruments. Indeed, downwelling SW irradiance was 120.2 W m$^{-2}$ for MR-40 and 117.8 W m$^{-2}$ for CNR4, equivalent to a +2 % difference. The systematic difference between both instruments was opposite for upwelling SW: MR-40 recorded 90.8 W m$^{-2}$ on average, whereas CNR4 recorded 93.1 W m$^{-2}$ (−2.5 %).

Since the differences for downwelling and upwelling irradiances have opposite sign, we suggest that they are not due to actual differences between the MR-40 and CNR4. Rather, these differences most likely reflect actual signals, due for instance to different mounting of the instruments (shadow and height), or to different surface type. These differences are hard to disentangle, because MR-40 and CNR4 were not deployed under close enough mounting and environmental conditions.

#### *4.2.2 Surface albedo*

The median surface broadband albedo obtained from MR-40 and CNR4 falls within the 0.75–0.80 range (Fig. 7b), typical of dry snow-covered sea ice (*e.g.* Perovich and Grenfell, 1981). Due to differences in recorded downwelling and upwelling irradiances, retrieved albedos are significantly different at both MR-40 and CNR4 sites: 0.76±0.05 for MR-40 and 0.79±0.04 for CNR4.

The FieldSpec FR provides a spectral view of the surface albedo, for snow-covered and snow-free sea ice (Fig. 8). Snow-free sea ice was obtained by artificially removing snow around the measurement point. Measurements suggest that snow-covered sea ice albedo is lower than typical continental snow albedo values, yet with similar spectral shape. This is because the albedo integrates contributions from both snow and the sea ice below, which scatters light less efficiently than snow. The spectral albedo of the snow-free sea ice was 0.6–0.7 in the visible region, 0.1–0.4 in the near-infrared region typically <0.1 in the 1.5–2.0 μm range. In the visible window, albedo would be affected by multiple scattering of air bubbles and brine within the sea ice. In the near-infrared and shortwave infrared wavelengths, the albedo would be dominated by direct surface (Fresnel) reflection at the

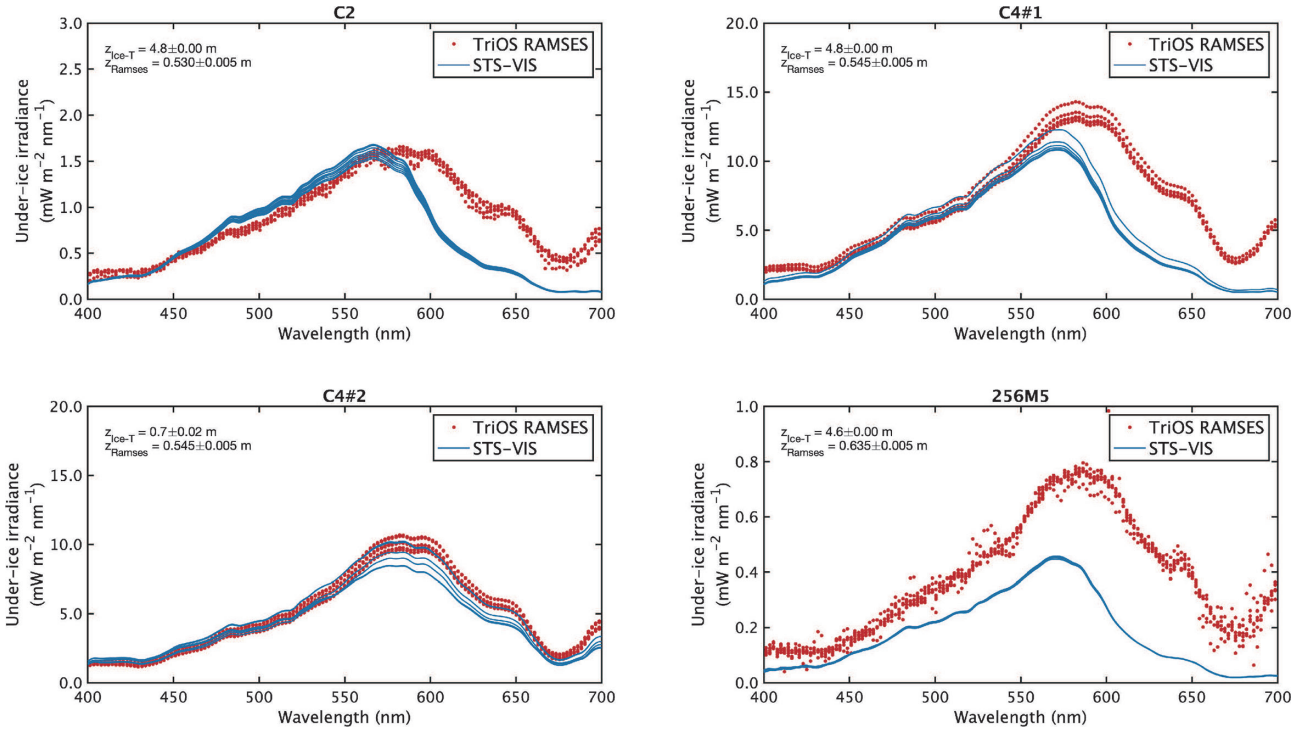


Fig. 9. Inter-comparison of transmitted irradiance measurements from STS-VIS (grey) and TriOS RAMSES (black) sensors. Note that $z_{Ice\text{-}T}$ and $z_{Ramses}$ are sensor positions and were measured from the air–ice interface.

sea ice surface, because of the relatively strong light absorption at such wavelengths.

### *4.3 Under-ice measurements: irradiance and transmittance*

#### *4.3.1 Inter-comparison of TriOS RAMSES and STS-VIS spectrometers*

On four occasions, the TriOS RAMSES and STS-VIS were jointly deployed at close locations and environments, for inter-comparison. The transmitted spectral irradiance recorded by both instruments is depicted in Fig. 9. During each session, several acquisitions were performed, indicating measurement uncertainty associated with small variations in sensor position.

For three of the four inter-comparison cases (C2, C4#1, 256M5), the depth of the Ice-T *fish* was left at its standard depth of deployment (about 5 m), whereas the TriOS RAMSES on its L-arm was held at about 0.5 m (0.075 m below the ice-ocean interface) (Fig. 9). In these three instances, the STS-VIS spectrum typically shows smaller red-light intensity than the TriOS RAMSES device, consistently with attenuation of irradiance with depth, stronger in seawater for red than for blue light. For the C4#2 deployment, the Ice-T *fish* was brought to about 70 cm depth, much closer to the TriOS RAMSES. In that case, both spectrometers give very close results. All in all, this exercise suggests that within uncertainties in spectral irradiance (about 1 mW m$^{-2}$ nm$^{-1}$), both instruments can be used interchangeably.

#### *4.3.2 Broadband irradiance*

The time series of under-ice irradiance, as recorded by STS-VIS, show a diurnal cycle of under-ice irradiance synchronized with surface irradiance (Fig. 7a). The recorded under-ice irradiance was within the range of $10^{-4}$—2 W m$^{-2}$. Transmittance was within the range of 0.1–0.5 % at 5 m depth.

#### *4.3.3 Spectral irradiance, transmittance and chl. a*

Both STS-VIS and Trios RAMSES consistently show under-ice light spectra typical of high-chlorophyll conditions, with irradiance peak shifted towards 550–600 nm. Under-ice spectral shape was independent of location (Trios RAMSES) or time of the day (STS-VIS). Spectral irradiance was within the range of 0–20 mW m$^{-2}$ nm$^{-1}$.

Spectral transmittance of sea ice was <1 %. As 85–90 % of incoming visible light is reflected at the surface and that less than 1 % is transmitted under the ice, bout 10 % of the incoming light must be absorbed within snow and sea ice.

The pair measurements of hyperspectral normalized transmittance and chl. *a* are displayed in Fig. 10. Integrated chl. *a* was within the range of 6.8–29.4 mg m$^{-2}$, with a mean of 18.8±6.0 mg m$^{-2}$. Larger integrated chlorophyll is typically associated with more transmitted green light and less transmitted red light (Fig. 10). This is consistent with the arguments proposed by Mundy *et al.* (2007), based on observations from Arctic first-year landfast sea ice of the Canadian Arctic. Snow effects have their weakest spectral dependence on transmitted light within the range of 400–570 nm. In addition, chl. *a*, one of the major pigments of sea ice algae, has a distinct absorption band center at 440 nm.

## 5. Physical properties of under-ice water

Under-ice water environments are related to the sea ice growth/melt process, and may affect the amount of biomass at the bottom of sea ice. In this section, the programs and preliminary results from the physical oceanographic observations are described. The main purpose of the research was to evaluate the ice–ocean heat exchange associated with evolution of the fast ice in the Saroma-ko Lagoon. In addition, these measurements were experimental training and test for the Multidisciplinary drifting Observatory for the Study of Arctic Climate (MOSAiC) during the year-round expedition from 2019 to 2020 into the central Arctic.

To investigate thermodynamic features in the near-surface layer during ice formation, we created a 1 m× 1 m square pool at site Y1 and then deployed an autonomous temperature-profiling buoy (IceTC2/30, Marlin-Yug) at its corner (Fig. 11). The instrument is a 2 m-long thermistor chain, with a 20 cm constant interval, and transmits the data via the Iridium satellite at an hourly time interval. As one of the main observations, the turbulent heat flux in the ice-water boundary layer was directly measured with an eddy-covariance flux system, which consists of an acoustic Doppler velocimeter (Vector, Nortek) and a fast-response thermometer (Rinko-EC by JFE Advantech Inc.). The two fast sensors were linked with a cable to make synchronized data sampling. The eddy-covariance system was installed in an ice hole 15 cm in diameter at a place 1 m apart from the pool.

We also established a wind-insulating shelter, which was located 10 m aside the experimental pool. Inside the shelter, an ADCP (400 kHz AquaDopp profiler) was deployed to observe horizontal current at multi-depths (approximate 3, 5, and 7 m). We also conducted profiles with a CTD probe (RINKO profiler, JFE Advantech). The data acquisition was performed as daily routine during a period between 24 and 27 February 2019, and resulted in 17 vertical profiles.

The preliminary results are described in the following. Averaged vertical profiles from overall CTD casts suggest that the sea-ice melt water created a 1-m thick, strongly stratified layer at the top (Fig. 12). In the layer, water temperature is always higher than the freezing point (Fig. 12 a). Meanwhile, a vertical gradient in salinity determines the shallow, strong stratification, where salinity changes by more than 10 over 1 m water depth (Fig. 12b). In the experiment pool, where the water surface was exposed to the air, surface temperature was rather sensitive to the solar radiation (Fig. 13). Regularly, it attained its maximum around noon, and then dropped in a few hours. Solar-heated water remained for longer hours at depths a few tens of centimeter below the ice-water boundary. It is added that the density of chl. *a* is coincidently high in the surface stratified layer, reaching 6 $\mu$g L$^{-1}$ (Fig. 12d).

The eddy-covariance system, measuring temperature and velocity at approximately 1-m depth, shows recurrent events of upward turbulent heat transfer (Fig. 13 a). The events were quite intermittent, and occasionally reached 5–10 W m$^{-2}$. The most prominent peak was one that occurred around 22:00 on 26 February, achieving greater than 60 W m$^{-2}$ in magnitude. With respect to the horizontal current, we cannot say any conclusion at this point. That is, we did not find any prevailing current, nor

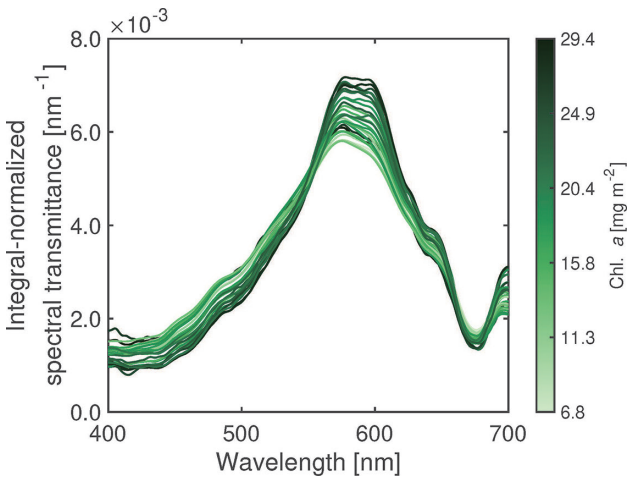


Fig. 10. Spectral transmittance measured by TriOS RAMSES ACC UV/VIS during SLOPE2019.

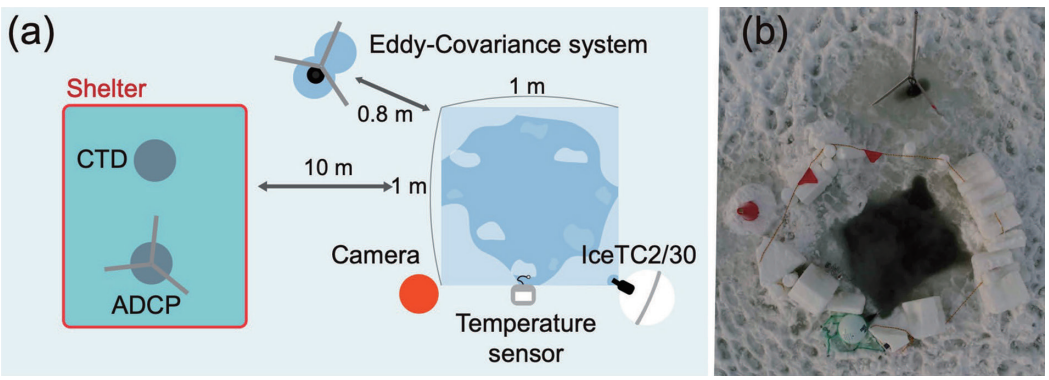


Fig. 11. Schematic view of upper-water thermodynamic experiment (a) and an aerial photograph of the site (b). The photo was taken by an air drone.

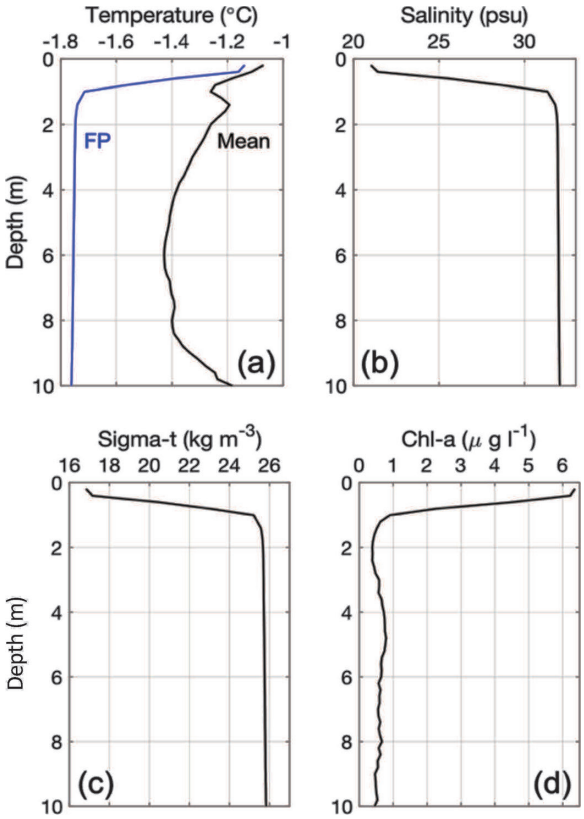


Fig. 12. Mean vertical profiles of the entire CTD observations for temperature (a) salinity (b) density anomaly $\sigma_T$ (c), and chl. *a* concentration. A blue solid line in (a) shows the freezing point, determined from the mean salinity profile in (b).

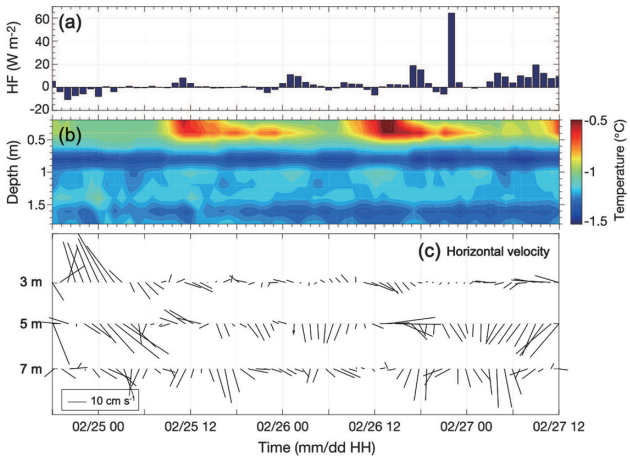


Fig. 13. Vertical turbulent heat flux measured by the eddy-covariance system (a). Temperature variation in the upper 2 m, recorded by the thermistor chain (b). Horizontal current velocity at depths of 3, 5, and 7 m (c). The length and direction of arrow indicate current speed and direction. The horizontal axis represents the local time. In panel (a), the upward heat flux is shown by positive sign, and the downward is vice versa.

tidal signals from the current data (Fig. 13c). The only notable exception was the northward current that happened during the evening of the first sampling day. The current was seen solely at 3 m depth, with nearly 20 cm $s^{-1}$ of magnitude. The northward flow could be related to the upward heat flux, being 5–10 W $m^{-2}$, which was observed by the eddy-covariance system at nearly same timing.

## 6. Artificial pool experiment

### *6.1 Effects of snow on the sea ice structure at the early growth stage*

To clarify the meteorological conditions which differentiate two crystal types of granular and columnar ice, and their formation processes especially for granular ice quantitatively, we made a square pool with a dimension of 1.5 m×1.5 m at 200 m away from the eastern shore of the Saroma-ko Lagoon and conducted field experiments to grow sea ice for the period from 25 to 27 February (Fig. 14). The salinity and depth of seawater at the pool were 31.2 psu and 1.2 m, respectively, and the pool was surrounded by 32 cm thick fast ice with 9 cm thick snow on it. The ice growth conditions were monitored with a camera mounted near the pool. The radiative fluxes were measured with a radiometer equipped near the AWS.

Fig. 14. Photographs of pool experiments for the whole site to examine the effects of snow on the sea ice structure at the early growth stage (a), where a white circle denotes a monitoring camera, and ice sampling (b).

During the period, relatively cold and calm conditions prevailed, which provided a favorable condition for the bottom freezing rather than frazil ice production. Instead, the difference in snowfall conditions provided a good opportunity to examine the effect of snow on the sea ice structure and surface heat balance at the early growth stage. We intend to estimate it quantitatively as a case study through the sample analysis and a thermodynamic ice-growth model.

### *6.2 Gas exchange process at the ice-free water surface*

Recent $CO_2$ flux measurements on sea ice indicate that sea ice is an active component in gas exchange between ocean and atmosphere (Delille *et al.*, 2014). In this campaign, we tried to set up and measure the $CH_4$ flux on sea ice in addition to the $CO_2$. A LI-COR 8100-104 chamber was installed within the 1 m×1.5 m artificial

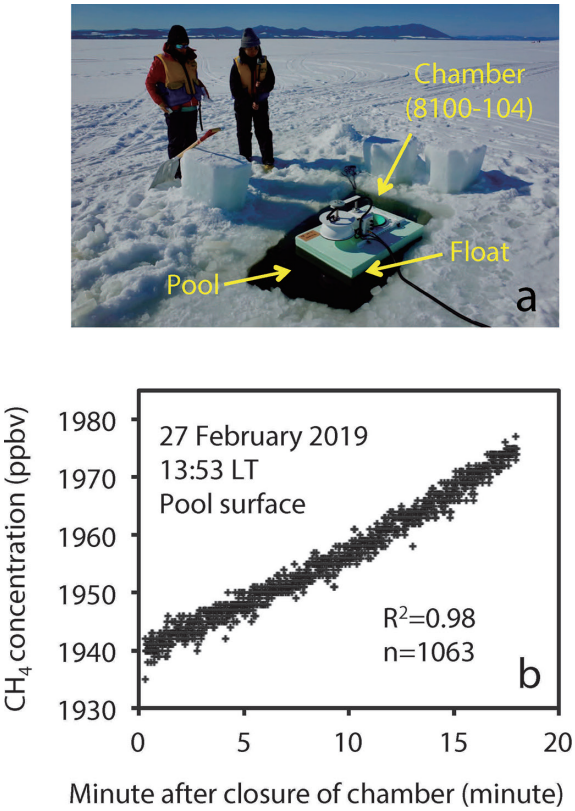


Fig. 15. Photograph of the $CO_2$ and $CH_4$ flux chamber system at an artificial pool site to compare the gas exchange process over the sea ice (a). Example of the temporal variation in $CH_4$ concentration in the chambers installed over the snow at 13:53 LT 27 February 2019 (b).

pool with float (Fig. 15a) from 12:00 to 16:00 27 February 2019. The chamber was connected to a LI-8100 A soil $CO_2$ flux system (LI-COR Inc.) for $CO_2$ and Ultraportable Greenhouse Gas Analyzer (Los Gatos Research) for $CH_4$ concentration within chamber. The $CO_2$ and $CH_4$ flux (mmol C $m^{-2}$ $day^{-1}$ for $CO_2$ and μmol C $m^{-2}$ $day^{-1}$ for $CH_4$) (positive value indicates $CO_2$ and $CH_4$ being released from ice surface to air) was calculated based on the changes of the $CO_2$ and $CH_4$ concentrations within the headspace of the chamber (Fig. 15b). This chamber deployment was also examined over the snow and after removing snow at site C2 at same time period (12:00 to 16:00) at 26 and 27 February, respectively. These measurements were training and test for MOSAiC.

For $CO_2$ flux, the mean (and standard deviation) values within the pool were −0.9±0.9 mmol C $m^{-2}$ $day^{-1}$ (n=12) and the magnitude of negative flux was higher than those measured over the snow (−0.6±0.3 mmol C $m^{-2}$ $day^{-1}$) (n=7) and the sea ice after removing snow (−0.8±0.3 mmol C $m^{-2}$ $day^{-1}$) (n=11) at site C2. These values and relationships between surface conditions for $CO_2$ flux were similar to those obtained in the previous study in the Saroma-ko Lagoon (Nomura *et al.*, 2010). For $CH_4$ flux, the mean (and standard deviation) values within the pool were +34.9±9.4 μmol C $m^{-2}$ $day^{-1}$ (n=12) and magnitude of positive flux was higher than those measured over the snow +0.1±0.9 μmol C $m^{-2}$ $day^{-1}$) (n=7) and the sea ice after removing snow (+0.7±1.7 μmol C $m^{-2}$ $day^{-1}$) (n=11) at site C2. These results suggested that the ice-free surface acts as sink for $CO_2$ and source for $CH_4$ because $CO_2$ and $CH_4$ concentration would be low and high with respect to that in the atmosphere, respectively (DIC/TA for $CO_2$ and $CH_4$ concentration measurement are currently being processed and analyzed). The results obtained during this campaign will become comparison data with respect to the data that will be obtained during MOSAiC.

## Acknowledgments

We would like to express heartfelt thanks to Saroma Research Center of Aquaculture and Napal Kitami for their support in conducting the field work. This work was supported by the Japan Society for the Promotion of Science (17H04715, 17K00534, 18H03745, 18KK0292, and 18F18794), the Grant for Joint Research Program of the Institute of Low Temperature Science, Hokkaido University, the Grant for Arctic Challenge for Sustainability, Joint Research Program of the Japan Arctic Research Network Center and the Grant for the Global Environmental Research Coordination System from Ministry of the Environment of Japan in FY2017, and the EU FP7 BISICLO project. This paper is a contribution to the SCOR Working Group 152–Measuring Essential Climate Variables in Sea Ice (ECV-Ice) and Biogeochemical Exchange Processes at Sea-Ice Interfaces (BEPSII).

## References

Arrigo, K.R. (2017): Sea ice as a habitat for primary producers. In D.N. Thomas (ed.), Sea Ice, 352–369, John Wiley & Sons, Ltd, doi: 10.1002/9781118778371.ch14.

Campbell, K., Mundy, C., Barber, D. and Gosselin, M. (2015): Characterizing the sea ice algae chlorophyll a–snow depth relationship over Arctic spring melt using transmitted irradiance. *J. Mar. Sys.*, **147**, 76–84, doi:10.1016/j.jmarsys.2014.01.008.

Delille, B., Vancoppenolle, M., Geilfus, N.-X., Tilbrook, B., Lannuzel, D., Schoemann, V., Becquevort, S., Carnat, G., Delille, D., Lancelot, C., Chou, L., Dieckmann, G. S. and Tison, J.-L. (2014): Southern Ocean $CO_2$ sink: the contribution of the sea ice. *J. Geophys. Res.: Oceans*, **119**, 6340–6355, doi:10.1002/2014JC009941.

Fierz, C., Armstrong, R. L., Durand, Y., Etchevers, P., Greene, E., McClung, D. M., Nishimura, K., Satyawali, P. K. and Sokratov, S. A. (2009): The international classification for seasonal snow on the ground. Tech. Rep., 90 pp., IHP-VII Technical Documents in Hydrology No. 83, IACS Contribution No. 1, UNESCO-IHP, Paris.

Granskog, M.A., Kaartokallio, H., Kuosa, H., Thomas, D.N., Ehn, J. and Sonninen, E. (2004): Scales of horizontal patchiness in chlorophyll a, chemical and physical properties of landfast sea ice in the Gulf of Finland (Baltic Sea). *Polar Biol.*, **28** (4), 276–283, doi:10.1007/s00300-004-0690-5.

Horner, R.A., Syvertsen, E.E., Thomas, D.P. and Lange, C. (1988): Proposed terminology and reporting units for sea ice algal assemblages. *Polar Biol.*, **8** (4), 249–253, doi:10.1007/bf00263173.

Kuchiki, K., Aoki, T., Niwano, M., Matoba, S., Kodama, Y. and

Adachi, K. (2015): Elemental carbon, organic carbon, and dust concentrations in snow measured with thermal optical and gravimetric methods: Validations during the 2007–2013 winters at Sapporo, Japan. *J. Geophys. Res.: Atmos.*, **120**, doi: 10.1002/2014JD022144.

Lange, B.A, Katlein, C, Nicolaus, M, Peeken, I. and Flores, H. (2016) Sea ice algae chlorophyll a concentrations derived from under- ice spectral radiation profiling platforms. *J. Geophys. Res.: Oceans*, **121** (12), 8511–8534, ISSN 2169–9291, doi:10.1002/2016JC011991.

Liu, Y, Saitoh, S. I., Maekawa, K., Mochizuki, K. I. and Tian, Y. (2018): Impact of short-term climate effects and sea ice coverage variation on Japanese scallop aquaculture in Saroma Lake, Japan. *Aquacult. Res.*, **49** (5), 1752–1767, doi: 10.1111/are.13630.

Lund-Hansen, L.C. and 6 others (2018): A low-cost remotely operated vehicle (ROV) with an optical positioning system for under-ice measurements and sampling. *Cold Reg. Sci. Technol.*, **151**, 148–155, doi:10.1016/j.coldregions.2018.03.017.

Melbourne-Thomas, J., Meiners, K., Mundy, C., Schallenberg, C., Tattersall, K. and Dieckmann, G. (2016): Corrigendum: Algorithms to estimate Antarctic sea ice algal biomass from under-ice irradiance spectra at regional scales. *Mar. Ecol.: Prog. Ser.*, **561**, 261.

Miller, L. A., Fripiat, F., Else, B. G. T., Bowman, J. S., Brown, K. A., Collins, R. E., Ewert, M., Fransson, A., Gosselin, M., Lannuzel, D., Meiners, K. M., Michel, C., Nishioka, J., Nomura, D., Papadimitriou, S., Russell, L. M., Sørensen, L. L., Thomas, D. N., Tison, J.-L., van Leeuwe, M. A., Vancoppenolle, M., Wolff, E. W. and Zhou, J. (2015): Methods for Biogeochemical Studies of Sea Ice: The State of the Art, Caveats, and Recommendation. *Elementa-Science of the Anthropocene*, **3**, 000038, doi:10.12952/journal.elementa.000038.

Mundy, C. J., Ehn, J. K., Barber, D. G. and Michel, C. (2007): Influence of snow cover and algae on the spectral dependence of transmitted irradiance through Arctic landfast first-year sea ice. *J. Geophys. Res.*, **112**, C03007, doi:10.1029/2006JC003683.

Nishi, Y. and Tabeta, S. (2005): Analysis of the contribution of ice algae to the ice-covered ecosystem in Lake Saroma by means of a coupled ice–ocean ecosystem model. *J. Mar. Sys.*, **55** (3–4), 249–270, doi:10.1016/j.jmarsys.2004.08.002.

Nomura, D., Takatsuka, T., Ishikawa, M., Kawamura, T., Shirasawa, K. and Yoshikawa-Inoue, H. (2009): Transport of chemical components in sea ice and under-ice water during melting in the seasonally ice-covered Saroma-ko Lagoon, Hokkaido, Japan. *Estuarine, Coastal Shelf Sci.*, **81**, 201–209, doi:10.1016/j.ecss.2008.10.012.

Nomura, D., Yoshikawa-Inoue, H., Toyota, T. and Shirasawa, K. (2010): Effects of snow, snow melting and refreezing processes on air–sea-ice $CO_2$ flux. *J. Glaciol.*, **56** (196), 262–270, doi:10.3189/002214310791968548.

Nomura, D., McMinn, A., Hattori, H., Aoki, S. and Fukuchi, M. (2011): Incorporation of nitrogen compounds into sea ice from atmospheric deposition. *Mar. Chem.*, **127**, 90–99, doi:10.1016/j.marchem.2011.08.002.

Perovich, D. K. and Grenfell, T. C. (1981): Laboratory studies of the optical properties of young sea ice. *J. Glaciol.*, **27**, 331–346, doi:10.3189/S0022143000015410.

Robineau, B., Legendre, L., Kishino, M. and Kudoh, S. (1997): Horizontal heterogeneity of microalgal biomass in the first-year sea ice of Saroma-ko Lagoon (Hokkaido, Japan). *J. Mar. Sys.*, **11** (1–2), 81–91, doi:10.1016/s0924–7963(96)00030–9.

Roukaerts, A., Nomura, D., Deman, F., Hattori, H., Dehairs, F. and Fripiat, F. (2019): The effect of melting treatments on the assessment of biomass and nutrients in sea ice (Saroma-ko lagoon, Hokkaido, Japan). *Polar Biol.*, **42**, 347–356, doi:10.1007/s00300–018–2426-y.

Shirasawa, K. and Leppäranta, M. (2003): Hydrometeorological and sea ice conditions at Saroma-ko lagoon, Hokkaido, Japan. In: Report Series in Geophysics. University of Helsinki, Finland No. 46, 161–168.

Shirasawa, K., Leppäranta, M., Saloranta, T., Kawamura, T., Polomoshnov, A. and Surkov, G. (2005): The thickness of coastal fast ice in the Sea of Okhotsk. *Cold Reg. Sci. Technol.*, **42**, 25–40, doi:10.1016/j.coldregions.2004.11.003.

Tanikawa, T., Hori, M., Aoki, T., Hachikubo, A., Kuchiki, K., Niwano, M., Matoba, S., Yamaguchi, S. and Stamnes, K. (2014): In situ measurements of polarization properties of snow surface under the Brewster geometry in Hokkaido, Japan, and northwest Greenland ice sheet. *J. Geophys. Res.: Atmos.*, **119,** 13,946–13,964, doi:10.1002/2014JD022325.

Uusikivi, J., Vahatalo, A.V., Granskog, M.A. and Sommaruga, R. (2010): Contribution of mycosporine-like amino acids and colored dissolved and particulate matter to sea ice optical properties and ultraviolet attenuation. *Limnol. Oceanogr.*, **55** (2), 703–713, doi:10.4319/lo.2010.55.2.0703.

Vancoppenolle, M., Meiners, K. M., Michel, C., Bopp, L., Brabant, F., Carnat, G., Delille, B., Lannuzel, D., Madec, G., Moreau, S., Tison, J.-L. and van der Merwe, P. (2013): Role of sea ice in global biogeochemical cycles: emerging views and challenges. *Quat. Sci. Rev.*, **79**, 207–230, doi:10.1016/j.quascirev.2013.04.011.

Wongpan, P., Meiners, K. M., Langhorne, P. J., Heil, P., Smith, I. J., Leonard, G. H., Massom, R. A., Clementson, L. A. and Haskell T. G. (2018): Estimation of Antarctic land-fast sea ice algal biomass and snow thickness from under-ice radiance spectra in two contrasting areas. *J. Geophys. Res.: Oceans*, **123**, 1907–1923, doi:10.1002/2017JC013711.